This is the accepted manuscript made available via CHORUS. The article has been published as:

Improved lattice Boltzmann modeling of binary flow based on the conservative Allen-Cahn equation

Feng Ren, Baowei Song, Michael C. Sukop, and Haibao Hu

Phys. Rev. E **94**, 023311 — Published 17 August 2016

DOI: 10.1103/PhysRevE.94.023311

Improved Lattice Boltzmann modeling of binary flow based on the conservative Allen-Cahn equation

Feng Ren[1, 2,*], Baowei Song[1], Michael C. Sukop[2,†], Haibao Hu[1]

1 School of Marine Science and Technology, Northwestern Polytechnical University, Xi'an, Shaanxi 710072, China

2 Department of Earth and Environment, Florida International University, 11200 SW 8th Street, Miami, FL 33199, USA

The primary and key task of binary fluid flow modeling is to track the interface with good accuracy, which is usually challenging due to the sharp interface limit and numerical dispersion. This article concentrates on further development of the conservative Allen-Cahn equation (ACE) [Geier *et al*., Phys. Rev. E **91**, 063309 (2015)] under the framework of the Lattice Boltzmann method (LBM), with incorporation of the incompressible hydrodynamic equations [Liang *et al*., Phys. Rev. E **89**, 053320 (2014)]. Utilizing a modified equilibrium distribution function and an additional source term, the new model is capable of correctly recovering the conservative ACE through the Chapman-Enskog analysis. We also simulate four phase-tracking benchmark cases, including one three-dimensional case; all show good accuracy as well as low numerical dispersion. By coupling the incompressible hydrodynamic equations, we also simulate layered Poiseuille flow and the Rayleigh-Taylor instability, illustrating satisfying performance in dealing with complex flow problems, e.g., high viscosity ratio, high density ratio, and high Reynolds number situations. The present work provides a reliable and efficient solution for binary flow modeling.

PACS number(s): 47.11.-j, 68.03.-g, 47.55.-t

I. INTRODUCTION

Binary fluid flows are nearly ubiquitous in nature and are of great significance in both scientific and industrial fields, e.g., porous media flow [1], surface wetting [2,3], droplet/bubble dynamics [4], etc. Many methods have been developed to numerically simulate these phenomena [5], typical methods including the volume of fluid method [6], the level set method [7], the front tracking method [8], the phase field method [9,10], and semi-Lagrangian-based methods [11], etc. Different from methods that mainly involve external advection, e.g., the volume of fluid method and the level set method, the phase field method applies a diffusion term to incorporate the motion of interfaces. Moreover, the analytical interface profile along the normal direction can be given initially, and it does not require interface construction like the volume of fluid method. In binary flow situations, especially when the surface tension has considerable effects [10], the phase field method has shown great advantage and enormous application potential.

The most frequently adopted governing equation of the phase field method is the Cahn-Hilliard equation (CHE) [12] that applies the chemical potential in the diffusion term. One key drawback of the CHE is that special treatment has to be done for this fourth-order term. Another strategy is to solve the conservative ACE. The original ACE was not globally conservative, but Chiu and Lin [13] derived the conservative form to preserve the total mass, based on the work of Sun and Beckermann [14] that modified the original ACE to a curvature-driven phase field model. By

*renfeng926@126.com
†sukopm@fiu.edu

contrast, the conservative ACE is much simpler than the CHE, especially in that only a second-order algorithm is needed for the discretization of the diffusion term.

In order to solve governing equations of the phase field method, in addition to the finite difference method (FDM) and the finite volume method [15] that are often used in computational fluid dynamics, the Lattice Boltzmann method (LBM) has revealed good performance and superior parallel efficiency in the past years [16–18]. He *et al.* [19] first introduced an additional equation for phase tracking, where the Carnahan-Starling equation of state was applied to derive the chemical potential in the CHE. Instead of the non-ideal gas equation, Lee and Lin [20] then applied the free energy scheme. However, these models share the drawback of not being able to recover the correct CHE. Later on, Zheng *et al.* [21,22] introduced a spatial difference term of the distribution function to recover the correct form of the CHE. Similarly, Zu *et al.* [23] rewrote the equilibrium distribution function and also recovered the correct CHE. Different from previous work, Liang *et al.* [24–26] also recovered the correct CHE by introducing a new equilibrium distribution function, together with an additional temporal term.

In terms of the conservative ACE, Geier *et al*. [27,28] first proposed the single-relaxation-time (SRT) algorithm, and showed better accuracy and better convergence rate over the CHE. Moreover, they offered an alternative algorithm to calculate the interface curvature locally, which greatly reduced computational expense but meanwhile brought an accuracy loss.

Based on the phase field method, the interfaces can be tracked with good accuracy, and by coupling the hydrodynamic equations, solutions for simulating binary flow systems are provided. Although many models are proposed for incorporating the hydrodynamic evolution, most of them cannot recover the correct incompressible Navier-Stokes (NS) equations. Based on the single-phase incompressible LBE [29], Zu *et al.* [23] solved this problem by introducing a velocity-based evolution procedure, different from previous momentum-based ones. However, since implicit schemes are utilized to calculate macroscopic velocity and pressure, a prediction-correction step is also required. Further, Liang *et al.* [24] proposed a new and simple evolution model that is also capable of correctly recovering the incompressible Navier-Stokes equations, while inheriting the advantages of typical Lattice Boltzmann (LB) models in simplicity and locality.

In the work reported herein, we propose an improved LB equation that correctly recovers the conservative ACE through the Chapman-Enskog analysis. To solve binary flow problems, we couple the incompressible hydrodynamic equation by Liang *et al.* [24] with necessary modifications.

This article is outlined as follows: in Sec. II, the methodology is introduced; in Sec. III, phase-tracking tests are conducted; in Sec. IV, two typical multiphase flow cases are conducted and analyzed; and in Sec. V, a brief summary is drawn.

II. METHODOLOGY

A. Conservative ACE

In Eulerian methods, the general advection equation is expressed as

$$\partial_t \phi + \mathbf{u} \cdot \nabla \phi = 0 , \tag{1}$$

where ϕ is the order parameter. Now we split the velocity vector into a normal speed u_n,

and an external velocity vector $\mathbf{u}_e$ [13,14], i.e., $\mathbf{u} = u_n\mathbf{n} + \mathbf{u}_e$. Herein the normal vector is calculated as $\mathbf{n} = \nabla\phi/|\nabla\phi|$, and then we have

$$\partial_t\phi + \mathbf{u}_e \cdot \nabla\phi + u_n|\nabla\phi| = 0. \tag{2}$$

From the viewpoint of the level set method [14,30], we can assume that the normal speed is proportional to the curvature, i.e., $u_n = -M_\phi\kappa$. Here M_ϕ is positive and is defined as the mobility. $\kappa = \nabla \cdot \mathbf{n}$ is the curvature. Hence, Eq. (2) can be further written as

$$\partial_t\phi + \mathbf{u}_e \cdot \nabla\phi = M_\phi(\nabla \cdot \mathbf{n})|\nabla\phi| = M_\phi\left(\nabla^2\phi - \mathbf{n} \cdot \nabla|\nabla\phi|\right). \tag{3}$$

Now we introduce the one-dimensional equilibrium profile for the order parameter ϕ along the z direction [10], i.e.,

$$\phi(z) = \frac{\phi_A + \phi_B}{2} + \frac{\phi_A - \phi_B}{2}\tanh\left(\frac{2z}{W}\right), \tag{4}$$

where W is the interfacial width, ϕ_A and ϕ_B are phase indicators for phase A and phase B, respectively. From Eq. (4), we can easily obtain $\nabla\phi = \theta\mathbf{n}$, where the general form for θ is expressed as

$$\theta = \frac{-4(\phi - \phi_A)(\phi - \phi_B)}{W(\phi_A - \phi_B)}. \tag{5}$$

The equilibrium value for the right side of Eq. (3) becomes $M_\phi(\nabla \cdot \mathbf{n})|\nabla\phi| = M_\phi\theta\nabla \cdot \mathbf{n}$. By subtracting this equilibrium value from the right side of Eq. (3), we obtain

$$\partial_t\phi + \mathbf{u}_e \cdot \nabla\phi = M_\phi\left(\nabla^2\phi - \mathbf{n} \cdot \nabla|\nabla\phi| - \theta\nabla \cdot \mathbf{n}\right). \tag{6}$$

If the term $\mathbf{n} \cdot \nabla|\nabla\phi|$ is also written with the equilibrium form, i.e., $\mathbf{n} \cdot \nabla\theta$, the right side of Eq. (6) would become $M_\phi\left[\nabla^2\phi - \nabla \cdot (\theta\mathbf{n})\right]$. By enforcing the divergence-free velocity condition, i.e., the incompressible continuity equation, we can obtain the conservative ACE, and it is expressed as

$$\partial_t\phi + \nabla \cdot (\phi\mathbf{u}_e) = M_\phi\left[\nabla^2\phi - \nabla \cdot (\theta\mathbf{n})\right]. \tag{7}$$

Note that the right-side term of Eq. (7) would become zero in the equilibrium state. Therefore, here the mobility acts as the rate towards the equilibrium state. In addition, the external velocity will be written as $\mathbf{u}$ in subsequent sections for simplification.

To obtain a non-dimensional form of Eq. (7), we define the dimensionless variables as

$$\bar{x}=\frac{x}{x^*},\ \bar{\mathrm{t}}=\frac{t}{t^*},\ \bar{\phi}=\frac{\phi}{\phi_A-\phi_B}. \tag{8}$$

Then Eq. (7) can be rewritten as

$$\partial_{\bar{t}}\bar{\phi}+\bar{\nabla}\cdot\left(\bar{\phi}\bar{\mathbf{u}}\right)=\frac{1}{Pe}\bar{\nabla}\left[\bar{\nabla}\bar{\phi}+\frac{4}{Ch}\left(\bar{\phi}-\bar{\phi}_A\right)\left(\bar{\phi}-\bar{\phi}_B\right)\mathbf{n}\right], \tag{9}$$

where $Pe=x^{*2}/\left(M_\phi t^*\right)$ is the Péclet number, and $Ch=W/x^*$ is the Cahn number.

In phase field theory, the more frequently used equation, i.e., the CHE, is expressed as

$$\partial_t\phi+\nabla\cdot\left(\phi\mathbf{u}\right)=\nabla\left(M_\phi\nabla\mu\right), \tag{10}$$

where $\mu(\phi)=\mu_0(\phi)-\kappa\nabla^2\phi=4\beta\left(\phi-\phi_A\right)\left(\phi-\phi_B\right)\left[\phi-\left(\phi_A+\phi_B\right)/2\right]-\kappa\nabla^2\phi$ is introduced as the chemical potential. Here β and κ are related to the surface tension coefficient σ and the interface width W, following the relationship

$$\beta=\frac{12\sigma}{W\left(\phi_A-\phi_B\right)^4},\ \text{and}\ \kappa=\frac{3\sigma W}{2\left(\phi_A-\phi_B\right)^2}. \tag{11}$$

Eq. (11) is obtained from the general phase-field theory and it is also available for the ACE. According to Eq. (4), we have $\nabla^2\phi=32\left(\phi-\phi_A\right)\left(\phi-\phi_A\right)\left[\phi-\left(\phi_A+\phi_B\right)/2\right]/\left[W^2\left(\phi_A-\phi_B\right)^2\right]$ in the equilibrium state. According to the definition of Eq. (11), the chemical potential would also become zero in the equilibrium state. Here the mobility acts as the rate towards the equilibrium value of chemical potential. Using the same dimensional variables as in Eq. (8), the dimensionless form of the CHE is written as

$$\partial_{\bar{t}}\bar{\phi}+\bar{\nabla}\cdot\left(\bar{\phi}\bar{\mathbf{u}}\right)=\bar{\nabla}\left\{\frac{1}{Pe}\bar{\nabla}\left[\frac{48}{Ch}\left(\bar{\phi}-\bar{\phi}_A\right)\left(\bar{\phi}-\bar{\phi}_B\right)\left(\bar{\phi}-\frac{\bar{\phi}_B+\bar{\phi}_B}{2}\right)-\frac{3Ch}{2}\bar{\nabla}^2\bar{\phi}\right]\right\}, \tag{12}$$

where $Pe=x^{*3}\left(\phi_A-\phi_B\right)^2/\left(M_\phi\sigma t^*\right)$, and $Ch=W/x^*$. Note that the definitions of the Péclet number for the CHE and the conservative ACE are quite different, especially in that for the conservative ACE, Pe is independent of the values of the phase indicators and the surface tension coefficient.

From Eq. (9) and Eq. (12), it is clear that the diffusion term contains fourth-order calculation in the CHE while only second-order calculation in the ACE. Moreover, based on the conservative ACE, analytical setup of the interfaces can be done geometrically, making simulations independent of chemical potential parameters that appear in the CHE.

B. LBM for the conservative ACE

In general, the LB evolution includes two individual processes, i.e., collision and streaming, and the two-step equation can be written as

$$\begin{cases} h_i'(\mathbf{x},t) = h_i(\mathbf{x},t) - \Lambda_{ij}\left(h_j(\mathbf{x},t) - h_j^{eq}\right) + \left(I_{ij} - \Lambda_{ij}/2\right)\left(S_i + R_i\right)\delta t \\ h_i\left(\mathbf{x} + \mathbf{e}_i\delta t, t + \delta t\right) = h_i'(\mathbf{x},t) \end{cases}, \tag{13}$$

where Λ_{ij} is an element of generalized collision matrix, h_i^{eq} is the equilibrium distribution function, and S_i and R_i are the source terms. In our scheme, the equilibrium function is expressed as

$$h_i^{eq} = w_i\phi\left(1 + \mathbf{e}_i \cdot \mathbf{u}/c_s^2\right), \tag{14}$$

where w_i is the weighing factor, i.e., $w_0 = 4/9$, $w_{1\sim4} = 1/9$, and $w_{5\sim8} = 1/36$ for the D2Q9 model. $\mathbf{e}$ is the lattice vector, and in the D2Q9 model, it is defined as

$$\mathbf{e} = c\begin{bmatrix} 0 & 1 & 0 & -1 & 0 & 1 & -1 & -1 & 1 \\ 0 & 0 & 1 & 0 & -1 & 1 & 1 & -1 & -1 \end{bmatrix}, \tag{15}$$

where $c = \delta x/\delta t$ is the lattice speed. c_s is the lattice sound speed, usually equaling $c/\sqrt{3}$. Note that in Eq. (14), high-order terms of velocity are canceled, thus resulting in the relationship $\sum h_i^{eq}\mathbf{e}_i\mathbf{e}_i = \phi c_s^2\mathbf{I}$. Through the Chapman-Enskog analysis shown in APENDIX A, we show that this change avoids a deviated term, i.e., $\nabla^2(\phi\mathbf{u}\mathbf{u})$.

The new source terms are defined as

$$S_i = w_i\theta\mathbf{e}_i \cdot \mathbf{n}, \text{ and} \tag{16}$$

$$R_i = \frac{w_i e_i \partial_t \phi\mathbf{u}}{c_s^2}. \tag{17}$$

Through the Chapman-Enskog analysis, we note that in the SRT algorithm by Geier *et al.* [27], another deviated term, i.e., $\nabla\left(1/s_3^h - 0.5\right)\partial_{t1}\phi\mathbf{u}$, would be introduced. And by using the source term of Eq. (17), this term would be eliminated and the correct conservative ACE can be recovered.

Based on Eq. (13), we further obtain the LBE using the multi-relaxation-time (MRT) algorithm, and it is expressed as

$$\mathbf{h}\left(\mathbf{x} + \mathbf{e}_i\delta t, t + \delta t\right) - \mathbf{h}\left(\mathbf{x},t\right) = -\mathbf{M}^{-1}\mathbf{\Lambda}^h\left[\mathbf{m}^h\left(\mathbf{x},t\right) - \mathbf{m}_{eq}^h\right] + \mathbf{M}^{-1}\left(\mathbf{I} - \mathbf{\Lambda}^h/2\right)\left(\mathbf{m}_S^h + \mathbf{m}_R^h\right)\delta t, \tag{18}$$

where $\mathbf{m}_{eq}^h = \mathbf{M}\mathbf{h}^{eq}$, $\mathbf{m}_S^h = \mathbf{M}\mathbf{S}^h$, and $\mathbf{m}_R^h = \mathbf{M}\mathbf{R}$ are the corresponding vectors in the moment space, respectively. $\mathbf{I}$ is the unit matrix and $\mathbf{\Lambda}^h = \left[s_0^h, s_1^h, s_2^h, \cdots, s_8^h\right]^T$ is the diagonal matrix. Here $s_3^h = s_5^h = 1/\tau^h$ and they are linked to the mobility through $M_\phi = \left(\tau^h - 0.5\right)c_s^2\delta t$. Note that the

mobility only depends on the value of the relaxation time, while in the methods that solve the CHE, the mobility usually depends on another parameter, e.g., in Ref. [24], $M_\phi = \eta\left(\tau^h - 0.5\right)c_s^2\delta t$, and η is used to tune the mobility.

If the computational domain is partitioned into a uniform Cartesian grid, we apply the FDM for the spatial gradient and divergence, wherein the second-order isotropic scheme is formulated as

$$\nabla\chi(\mathbf{x},t) = \frac{1}{c_s^2\delta t}\sum w_i\mathbf{e}_i\chi(\mathbf{x}+\mathbf{e}_i\delta t,t), \tag{19}$$

where χ can be any scalar. The temporal derivative in Eq. (17) is calculated by the first-order Eulerian scheme, i.e.,

$$\partial_t\chi = \frac{\chi(t)-\chi(t-\delta t)}{\delta t}. \tag{20}$$

C. LBM for the hydrodynamic equation

In the derivation of the conservative ACE, the divergence-free velocity field is incorporated as a premise. To keep consistent, we follow the LB hydrodynamic equation developed by Liang *et al.* [24], which is proven to be capable of recovering the incompressible NS equations correctly. The MRT scheme is expressed as

$$\mathbf{g}(\mathbf{x}+\mathbf{e}_i\delta t,t+\delta t)-\mathbf{g}(\mathbf{x},t) = -\mathbf{M}^{-1}\boldsymbol{\Lambda}^g\left[\mathbf{m}^g(\mathbf{x},t)-\mathbf{m}^g_{eq}(\mathbf{x},t)\right]+\mathbf{M}^{-1}\left(\mathbf{I}-\boldsymbol{\Lambda}^g/2\right)\mathbf{m}^g_S\delta t, \tag{21}$$

where $\mathbf{m}^g_{eq} = \mathbf{M}\mathbf{g}^{eq}$ and $\mathbf{m}^g_S = \mathbf{M}\mathbf{S}^g$ are expressed as

$$\mathbf{m}^h_{eq} = \left[0, \frac{2p+\rho\left(u_x^2+u_y^2\right)}{c_s^2}, -\frac{3p+\rho\left(u_x^2+u_y^2\right)}{c_s^2}, \frac{\rho u_x}{c}, -\frac{\rho u_x}{c}, \frac{\rho u_y}{c}, -\frac{\rho u_y}{c}, \frac{\rho\left(u_x^2-u_y^2\right)}{c^2}, \frac{\rho u_x u_y}{c^2}\right]^T, \quad \text{and} \tag{22}$$

$$\mathbf{m}^g_S = \begin{bmatrix} 3\mathbf{u}\cdot\nabla\rho c_s^2 \\ 6\mathbf{u}\cdot\mathbf{F}-9|\mathbf{u}|^2\,\mathbf{u}\left(\mathbf{F}+\nabla\rho c_s^2\right) \\ -6\mathbf{u}\cdot\mathbf{F}-3\mathbf{u}\cdot\nabla\rho c_s^2+9|\mathbf{u}|^2\,\mathbf{u}\left(\mathbf{F}+\nabla\rho c_s^2\right) \\ F_x \\ -F_x+3u_y^2\left(\mathbf{F}+\nabla\rho c_s^2\right)_x+6u_xu_y\left(\mathbf{F}+\nabla\rho c_s^2\right)_y \\ F_y \\ -F_y+3u_x^2\left(\mathbf{F}+\nabla\rho c_s^2\right)_y+6u_xu_y\left(\mathbf{F}+\nabla\rho c_s^2\right)_x \\ u_x\left(2+3u_y^2-3u_x^2\right)\left(\mathbf{F}+\nabla\rho c_s^2\right)_x+u_y\left(-2+3u_y^2-3u_x^2\right)\left(\mathbf{F}+\nabla\rho c_s^2\right)_y \\ u_y\left(1-3u_x^2\right)\left(\mathbf{F}+\nabla\rho c_s^2\right)_x+u_x\left(1-3u_y^2\right)\left(\mathbf{F}+\nabla\rho c_s^2\right)_y \end{bmatrix}, \tag{23}$$

where $\mathbf{F}=\left(F_x,F_y\right)=\mathbf{F}_s+\mathbf{G}+\mathbf{F}_a$ is the force vector. Here $\mathbf{F}_s$ is the surface tension force, $\mathbf{G}$ is the gravitational force. $\mathbf{F}_a$ is introduced by Li *et al.* [31] to eliminate an artificial interfacial force, and for the conservative ACE, this compensating force is formulated as

$$\mathbf{F}_a=q\mathbf{u}=d_\phi\rho\cdot M_\phi\left[\nabla^2\phi-\nabla\left(\theta\mathbf{n}\right)\right]\mathbf{u}. \tag{24}$$

The surface tension calculation follows the recommendation of Kim [32] and Chao *et al.* [33] as

$$\mathbf{F}_s=-\kappa\left|\nabla\phi\right|^2\mathbf{n}\nabla\cdot\mathbf{n}. \tag{25}$$

The macroscopic variables have the following explicit forms

$$\rho=\frac{\phi-\phi_B}{\phi_A-\phi_B}\left(\rho_A-\rho_B\right)+\rho_B, \tag{26}$$

$$\mathbf{u}=\frac{\sum\mathbf{e}_ig_i+0.5\left(\mathbf{F}_s+\mathbf{G}\right)}{\rho-0.5q},\ \text{and} \tag{27}$$

$$p=\frac{c_s^2}{1-w_0}\left[\sum_{i\neq0}g_i+\frac{1}{2}\mathbf{u}\cdot\nabla\rho-\frac{w_0}{2c_s^2}\rho\left|\mathbf{u}\right|^2\right]. \tag{28}$$

In order to avoid the sharp-interface limit of phase-field based models, we apply a step form for the dynamic viscosity, i.e.,

$$\mu=\begin{cases}\mu_A,\ \phi\geq0.5\left(\phi_A+\phi_B\right)\\ \mu_B,\ \phi<0.5\left(\phi_A+\phi_B\right)\end{cases}. \tag{29}$$

In the diagonal matrix $\mathbf{\Lambda}^g=\left[s_0^g,s_1^g,s_2^g,\cdots,s_8^g\right]^T$, we have $s_7^g=s_8^g=1/\tau^g$ and they are linked to the kinematic viscosity through $\nu=\left(\tau^g-0.5\right)c_s^2\delta t$.

III. PHASE-TRACKING TESTS

Our improved model (denoted as Model I) is compared with two models: the high-order FDM for the conservative ACE (denoted as Model II) and the original SRT model by Geier *et al.* [27] (denoted as Model III).

Regarding Model II, the fifth-order upwind weighed essentially nonoscillatory (WENO) scheme [34,35] is applied to discretize the convection term, and the third-order total variation diminishing (TVD) Runge-Kutta scheme [35,36] is employed to propagate in time. The fourth-order isotropic scheme [25] is used to calculate the spatial gradient and divergence in the diffusion term, which is formulated as

$$\nabla\chi\left(\mathbf{x},t\right)=\frac{1}{6c_s^2\delta t}\sum w_i\mathbf{e}_i\left[8\chi\left(\mathbf{x}+\mathbf{e}_i\delta t,t\right)-\chi\left(\mathbf{x}+2\mathbf{e}_i\delta t,t\right)\right], \tag{30}$$

where χ can be any scalar.

Four standard benchmark cases [23,24,27] are presented below, including diagonal translation of a circular interface, circular interface in a shear flow, smoothed deformation of a circular interface, and three-dimensional (3D) spherical interface in a shear flow, where special velocity fields that satisfy the divergent-free condition are given. According to the analysis of Eq. (9), we define the Péclet number as $Pe = U_0 L_0 / M_\phi$, where U_0 is the reference velocity, and L_0 is the side length of the square computational domain. We note that in Ref. [27], the interface width acts as the reference length, i.e., $Pe = U_0 W / M_\phi$. However, it is improper because a wider interface would enhance the numerical stability, while a larger Pe would bring an opposite effect. In addition, due to different definitions of Pe in the conservative ACE and the CHE, comparisons are not made in this article.

The Cahn number is defined as $Ch = W / L_0$. Moreover, we also study the effect of the Courant-Friedrichs-Lewy (CFL) number, which is defined as $CFL = U_0 \delta t / \delta x$. Here the time step δt and the grid size δx are both set to be unity. In addition, the phase indicators $\phi_A = 1$ and $\phi_B = 0$.

To evaluate the performance of the three models, we use the L_2-norm relative error of the order parameter between numerical and analytical results [23,24,27], i.e.,

$$\left\| \delta\phi \right\|_2 = \sqrt{\sum_{i,j} \left(\phi - \phi_0 \right)^2 \Big/ \sum_{i,j} \phi_0^2} \tag{31}$$

where ϕ_0 is the initial value of the order parameter that satisfies the equilibrium state in Eq. (4) along the normal direction of the interface.

Theoretically, in the equilibrium state, the maximum and minimum value of the order parameter would be limited to ϕ_A and ϕ_B, respectively. But in practice, this condition cannot be achieved due to numerical dispersion. Therefore, in order to evaluate the performance in light of numerical dispersion, relative maximum and minimum values of the order parameter are recorded respectively during the simulations, and they are shown as

$$\overline{\phi}_{\max} = \max \left\{ \frac{\phi_{i,j} - \phi_A}{\phi_A - \phi_B} \right\}, \text{ and } \overline{\phi}_{\min} = \min \left\{ \frac{\phi_B - \phi_{i,j}}{\phi_A - \phi_B} \right\}. \tag{32}$$

A. Diagonal translation of a circular interface

In this case, an initially circular interface with radius $R = L_0 / 4$ is placed in a periodic $L_0 \times L_0$ domain. The circular interface is driven by a uniform velocity field, i.e.,

$$\begin{cases} u_x(x,y) = U_0 \\ u_y(x,y) = U_0 \end{cases}. \tag{33}$$

Theoretically, after $T = L_0/U_0$ time steps, the interface would translate to the original position and coincide with the initial one. Based on this test, the effect of the CFL number and the convergence study are presented.

In order to evaluate the effect of the CFL number, we tune the value of U_0, while keeping fixed value of the Péclet number and the Cahn number at a grid resolution $L_0 = 128\,lu$. Herein lu represents the lattice length unit. Additionally, in subsequent sections, ts and mu represent the lattice time unit and mass unit, respectively. Results for the effect of the CFL number are shown in FIG. 1. Herein for Model II that applies the high-order FDM, the CFL number is limited to 0.1, thus the effect of the CFL number can be ignored, and the relative errors are independent of the CFL number. By comparison, from Model I, the effect of the CFL is minor, and the relative errors are even smaller than those calculated by Model II. Meanwhile, because Model III recovers an incorrect ACE, the relative error keeps increasing as the reference velocity increases.

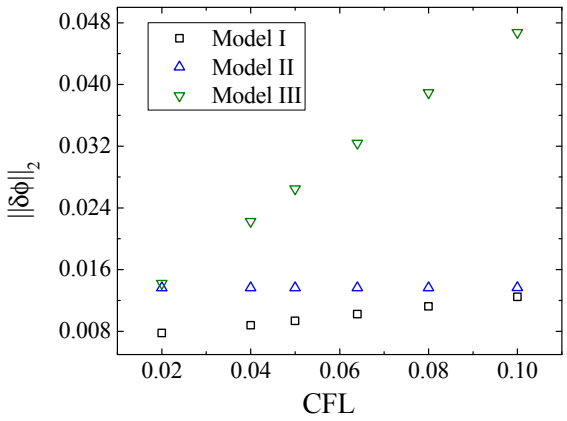

FIG. 1. Effect of the CFL number: L2-norm relative error for the diagonal translation of a circular interface at $Pe = 2,500$ and $Ch = 3/128$. Model I: our improved model; Model II: high-order FDM; Model III: method introduced by Geier *et al*.

In the convergence study, for the three individual schemes, we refine the grid while keeping constant Péclet number, Cahn number, and CFL number. Results are shown in FIG. 2, where both the horizontal and the vertical axis are logarithmic. Using a linear fitting method, the corresponding slopes are calculated, and the absolute values represent the convergence rate [27,37]. Generally the LBE is proven to be of second order while in practice the convergence rate is often less than two. Our results using Model I and Model III illustrate this point, and the convergence rate of Model I is almost twice that of Model III. For Model II, the convergence rate is right between that of the spatial and the temporal discretization order. Note that the results are quite different from Ref. [27], because

of different definitions of the Péclet number.

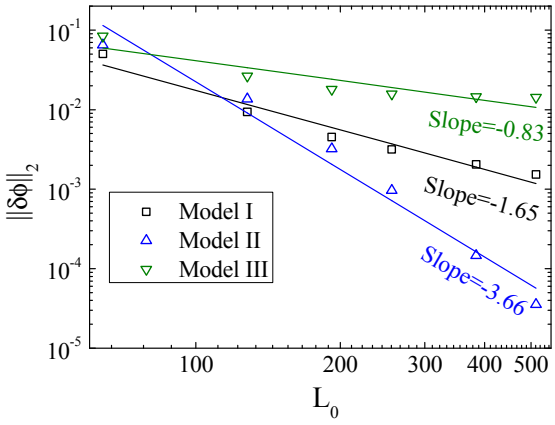

FIG. 2. Convergence study for the diagonal translation of a circular interface at $Pe = 2,500$, $Ch = 3/128$ and $CFL = 0.05$.

B. Circular interface in a shear flow

In this test, a circular interface with radius $R = L_0/5$ is initially placed at $x = L_0/2$ and $y = 3L_0/10$ in a periodic $L_0 \times L_0$ domain. The velocity field follows Eq. (34) [24,27] and its direction is reversed after $T/2$ time steps. Here the reference length is $L_0 = 256\,lu$ and the time period is $T = 2L_0/U_0$. After one period, the interface should rotate back to its original location. The interfaces at $\phi = (\phi_A + \phi_B)/2$ are shown in FIG. 3, where the rotation and deformation by all models are satisfying. However, based on the relative maximum values of the order parameter, shown in FIG. 4, Model III shows the worst performance in terms of numerical dispersion.

$$\begin{cases} u_x(x,y) = U_0\pi \cdot \sin\left(\dfrac{\pi x}{L_0}\right) \cdot \cos\left(\dfrac{\pi y}{L_0}\right) \\ u_y(x,y) = -U_0\pi \cdot \cos\left(\dfrac{\pi x}{L_0}\right) \cdot \sin\left(\dfrac{\pi y}{L_0}\right) \end{cases}. \tag{34}$$

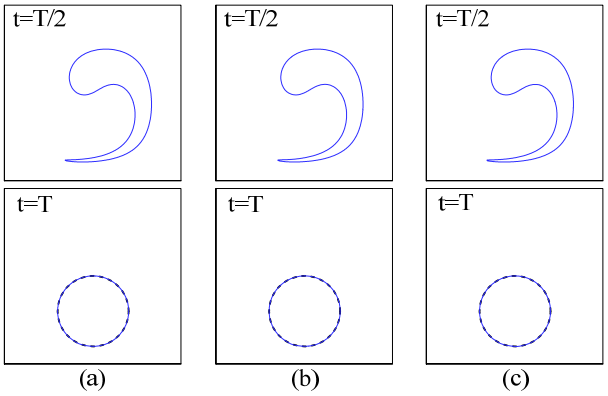

FIG. 3. Snapshots for circular interface in a shear flow at $Pe = 5,120$, $Ch = 3/256$ and $CFL = 0.02$. (a) Model I; (b) Model II; (c) Model III. Dashed lines at $t = T$ represent the initial shape.

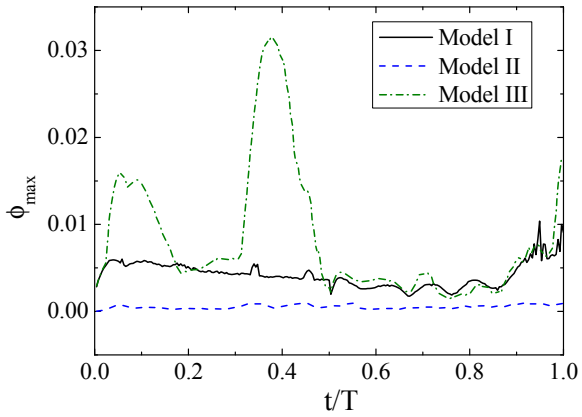

FIG. 4. Time evolution of relative maximum value of order parameter for circular interface in a shear flow at $Pe = 5,120$, $Ch = 3/256$ and $CFL = 0.02$.

For high values of the CFL number (shown in TABLE I), numerical instability occurs easily using Model III, while both Model I and Model II are almost not influenced. The conclusion is similar with that of the diagonal translation of a circular interface, but herein the flow field is much more complicated because of the rotating movement and the deformation.

It is also clearly shown in TABLE II that both Model I and Model III are not able to run at high Péclet numbers, suggesting that both models work in a limited range of Péclet number. Meanwhile, we note that Model II illustrates good performance for varying Péclet numbers. In fact, the high-order FDM model is even capable of solving the volume of fluid equation, which can be regarded as a special situation where the Péclet number becomes infinity.

TABLE I. Relative error for circular interface in a shear flow at $Pe = 5,120$ and $Ch = 3/256$.

Model	CFL			
	0.02	0.04	0.05	0.064
I	0.0200	0.0199	0.0198	0.0196

II	0.0228	0.0228	0.0228	0.0228
III	0.0171	unstable	unstable	unstable

TABLE II. Relative error for circular interface in a shear flow at $CFL = 0.02$ and $Ch = 3/256$.

Model	Pe			
	2,560	5,120	10,240	20,480
I	0.0126	0.0200	0.0326	0.138
II	0.0136	0.0228	0.0383	0.0573
III	0.0114	0.0171	0.0308	unstable

C. Smoothed deformation of a circular interface

In this test, a circular interface with radius $R = L_0/5$ is placed in a periodic $L_0 \times L_0$ domain. The velocity field follows Eq. (35) and here a temporal smoothing term, i.e., $\cos\left(\frac{\pi t}{T}\right)$, is applied to avoid sharp changes [24,27]. We set $L_0 = 512\,lu$ and $T = L_0/U_0$. In the first half-period, the interface deforms smoothly and forms thin filamentary structures. The second half-period witnesses a reversed deformation of the interface shape corresponding to the varying velocity field. The overall evolution process using the improved model (Model I) is depicted in FIG. 5, followed by final interface configurations in FIG. 6.

$$\begin{cases} u_x(x,y) = -U_0 \cdot \sin\left(\frac{4\pi x}{L_0}\right) \cdot \sin\left(\frac{4\pi y}{L_0}\right) \cdot \cos\left(\frac{\pi t}{T}\right) \\ u_y(x,y) = -U_0 \cdot \cos\left(\frac{4\pi x}{L_0}\right) \cdot \cos\left(\frac{4\pi y}{L_0}\right) \cdot \cos\left(\frac{\pi t}{T}\right) \end{cases}. \tag{35}$$

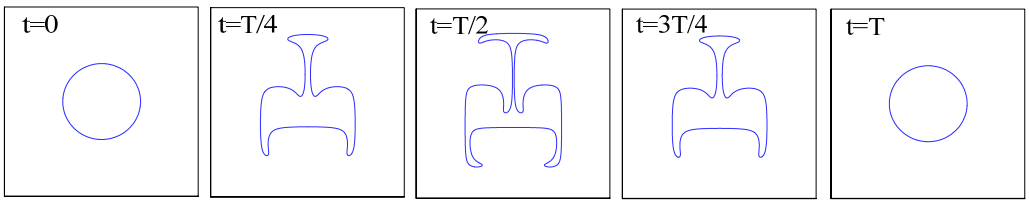

FIG. 5. Snapshots for smoothed deformation of a circular interface at $Pe = 10,240$, $Ch = 1/256$, and $CFL = 0.05$ using Model I.

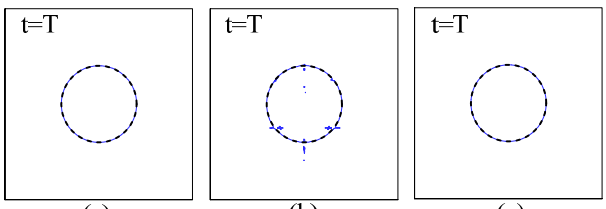

FIG. 6. Snapshots for smoothed deformation of a circular interface at $t = T$, $Pe = 10,240$, $Ch = 1/256$, and $CFL = 0.05$.

(a) Model I; (b) Model II; (c) Model III. Dashed lines represent the initial shape.

In addition, quantitative comparisons among the models are summarized in TABLE III and TABLE IV, illustrating effects of the CFL number and the Péclet number, respectively. The variation of the relative maximum error with time is shown in FIG. 7.

It is clear that in this deformation-dominated test (i.e., large gradient of any component of the velocity vector), Model II shows the worst performance, while Model I and Model III both attain good interface shapes and good accuracy. It is also noted that the calculated relative error of Model I and Model III are almost the same. Meanwhile, from the perspective of the numerical dispersion reflected in FIG. 7, our improved model reveals better performance, especially in the second half period.

TABLE III. Relative error for smoothed deformation of a circular interface at $Pe = 10,240$ and $Ch = 1/256$.

Model	CFL			
	0.02	0.04	0.05	0.064
I	0.0139	0.0142	0.0142	0.0144
II	0.104	0.102	0.104	0.106
III	0.0136	0.0136	0.0139	0.0143

TABLE IV. Relative error for smoothed deformation of a circular interface at $CFL = 0.05$ and $Ch = 1/256$.

Model	Pe			
	5,120	10,240	20,480	40,960
I	0.0120	0.0142	0.0326	0.0537
II	0.181	0.104	0.0770	0.0755
III	0.0141	0.0139	0.0319	0.0529

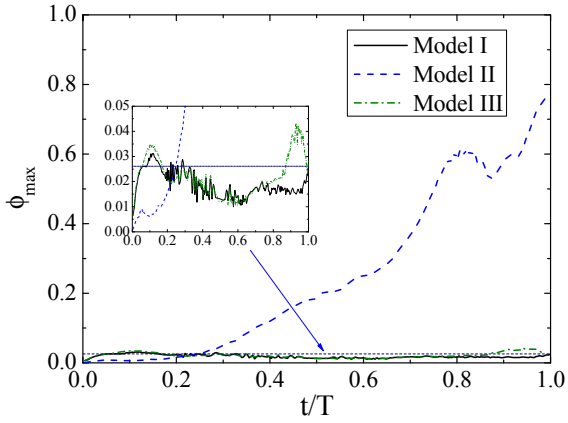

FIG. 7. Time evolution of relative maximum value of order parameter for smoothed deformation of a circular interface at $Pe = 10,240$, $Ch = 1/256$, and $CFL = 0.05$.

D. 3D spherical interface in a shear flow

In this section, we simulate a 3D spherical interface in a shear flow, i.e., the extension of 2D circular interface in a shear flow. Herein we adopt the D3Q15 model, and the 3D implementations of Model I can be found in APPENDIX B.

In this test, a spherical interface with radius $R = L_0/5$ is placed in a periodic $L_0 \times L_0 \times L_0$ domain. The velocity field is shown in Eq. (36) [22] and the direction is reversed after the first half-period. Here similar parameters are chosen as for the 2D case. We have $L_0 = 256\ lu$ and the period is also $T = 2L_0/U_0$. After one period, the interface should rotate back to its original location. Simulation results for the case at $Pe = 5,120$, $Ch = 3/256$, and $CFL = 0.02$ are shown in FIG. 8, which is shown from the isometric perspective. Here clear outlines of the interfaces are successfully obtained, even at the thin tails. And the relative error of the order parameter after one period equals 0.0273, close to that of the 2D case.

$$\begin{cases} u_x(x,y) = U_0\pi \cdot \cos\left(\dfrac{\pi x}{L_0} - \dfrac{\pi}{2}\right) \cdot \left[\sin\left(\dfrac{\pi y}{L_0} - \dfrac{\pi}{2}\right) - \sin\left(\dfrac{\pi z}{L_0} - \dfrac{\pi}{2}\right)\right] \\ u_y(x,y) = -U_0\pi \cdot \cos\left(\dfrac{\pi y}{L_0} - \dfrac{\pi}{2}\right) \cdot \left[\sin\left(\dfrac{\pi x}{L_0} - \dfrac{\pi}{2}\right) - \sin\left(\dfrac{\pi z}{L_0} - \dfrac{\pi}{2}\right)\right] \\ u_z(x,y) = -U_0\pi \cdot \cos\left(\dfrac{\pi z}{L_0} - \dfrac{\pi}{2}\right) \cdot \left[\sin\left(\dfrac{\pi y}{L_0} - \dfrac{\pi}{2}\right) - \sin\left(\dfrac{\pi x}{L_0} - \dfrac{\pi}{2}\right)\right] \end{cases}. \tag{36}$$

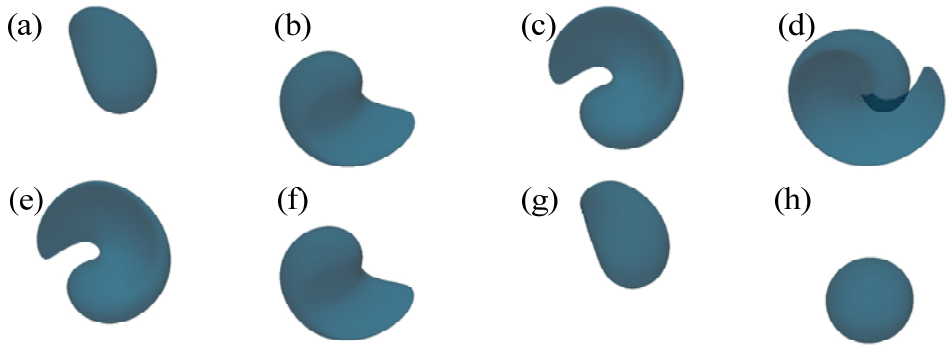

FIG. 8. Snapshots for 3D spherical interface in a shear flow using Model I at $Pe = 5,120$, $Ch = 3/256$, and $CFL = 0.02$. (a) to (h) represents $t = T/8$ to $t = T$, respectively.

From the above cases, we notice that while solving the conservative ACE, the conventional high-order FDM shows good performance but fails to simulate deformation-dominated flow like the smoothed deformation of a circular interface. Meanwhile, our improved model shows satisfying performance considering the effect of the CFL number and the Péclet number, the convergence rate,

and numerical dispersion. Due to the theoretically incorrect form of Model III, the independence of the CFL number cannot be achieved, and its performance in terms of numerical dispersion is not satisfying.

IV. BINARY FLOW TESTS

A. Layered Poiseuille flow

For immiscible binary flow between two parallel plates driven by a constant body force [17,23,38–40], the fluid flow is governed by the following equations

$$\mu_A \nabla^2 u_A = G, \text{ and } \mu_B \nabla^2 u_B = G. \tag{37}$$

where G is the driving body force, and μ_A and μ_B are the dynamic viscosities of the two fluids. An analytical solution can be derived by applying the non-slip wall boundary condition, and the continuous velocity and shear stress condition in the interfacial region [17,23], i.e.,

$$\begin{cases} u_A\big|_{y=0} = u_B\big|_{y=0} \\ \mu_A\left(\partial_y u_A\right)\big|_{y=0} = \mu_B\left(\partial_y u_B\right)\big|_{y=0} \\ u_A\big|_{y=a} = u_B\big|_{y=-a} = 0 \end{cases}. \tag{38}$$

In our simulation, the liquid phase flows in the region $0 < y \le a$ and the gas phase flows in the region $-a \le y < 0$. The grid resolution is 128×128. We set the density pair $\rho_A = \rho_B = 1\, mu/lu^3$. The dynamic viscosity ratio μ_A/μ_B equals 10 in Case A, 100 in Case B, and 1,000 in Case C, respectively, and we have $\mu_A = 0.005\, mu/(lu \cdot ts)$. The constant driving force is related to the central velocity, i.e., $u_c = Ga^2/(\mu_A + \mu_B)$, and we have $u_c = 0.0005\, lu/ts$. Velocity profiles are normalized by the central velocity and shown in FIG. 9. To be clear, the L_1-norm relative errors of numerical and analytical results [23], i.e., $|1 - u_{num}/u_{ana}| \times 100\%$, are shown in FIG. 10.

In the two cases, velocity profiles agree well with the analytical solutions, and the relative errors are below a very low level, i.e., 0.8%, and much smaller in non-boundary and non-interface regions. Hence, the numerical model appears to work very well for high viscosity ratio cases.

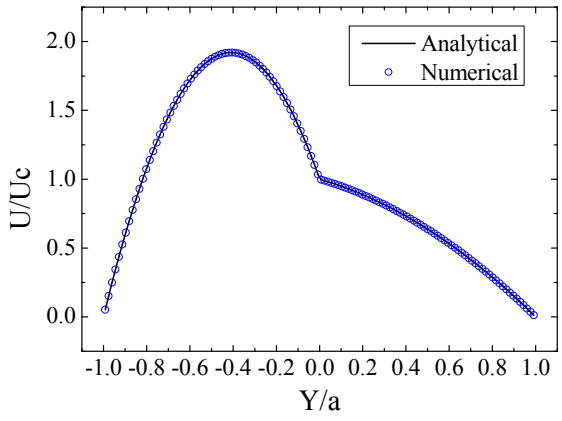

(a)

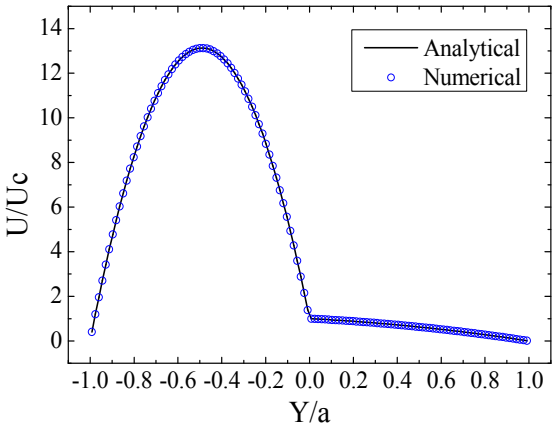

(b)

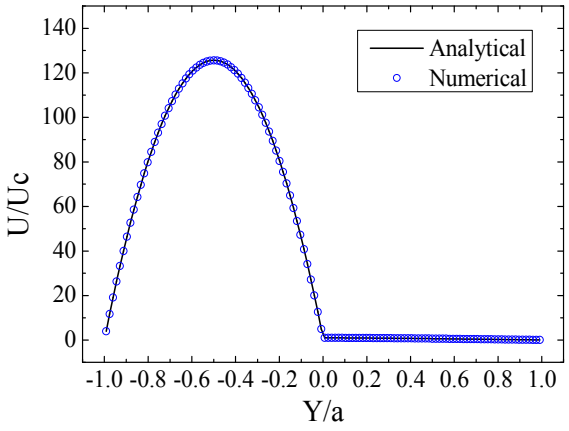

(c)

FIG. 9. Velocity profile of layered Poiseuille flow. (a) Case A: $\mu_A / \mu_B = 10$; (b) Case B: $\mu_A / \mu_B = 100$; (c) Case C: $\mu_A / \mu_B = 1,000$.

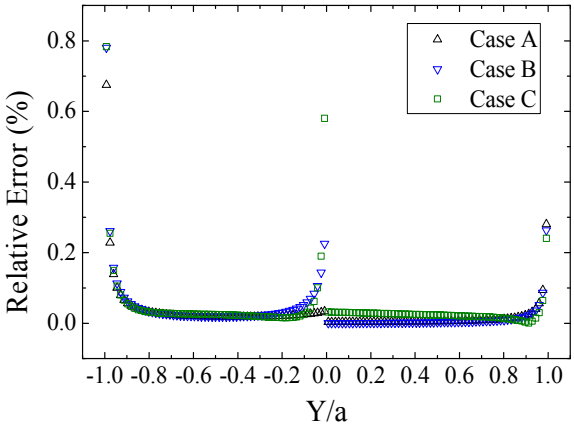

FIG. 10. Relative errors for layered Poiseuille flow. Case A: $\mu_A/\mu_B = 10$; Case B: $\mu_A/\mu_B = 100$; Case C: $\mu_A/\mu_B = 1,000$.

Previously, a dynamic viscosity ratio up to 1,000 was also achieved by Ginzburg [39] using a modified collision operator for the Richard's equation (for heterogeneous anisotropic aquifers), and Porter *et al.* [40], where the multi-component pseudopotential model was used. Since the algorithm, mesh resolution, and parameters adopted in different literatures are quite different, direct comparisons are hard to make. However, as far as we know, for most previous simulations concerning the layered Poiseuille flow, the calculated velocity profiles deviate from analytical ones at the interfacial region. Here our smaller L_1 – norm relative errors of numerical and analytical results in FIG. 10 show the benefit of this approach.

Based on the phase-field theory with a recovered CHE, Zu *et al.* [23] also conducted cases with $\mu_A/\mu_B = 1,000$, where the mixture dynamic viscosity is approximated by linearly interpolating the reciprocals of the dynamic viscosity of binary fluids. In our opinion, since the analytical velocity profile changes sharply across the interface, in order to avoid the limitation of diffusive interface, it is more reasonable to adopt sharp changing dynamic viscosity, as shown in Eq. 29.

B. Rayleigh-Taylor instability

Rayleigh-Taylor instability [23,24,31,37,41,42] is a type of flow instability that occurs when a heavy phase is on top of a light phase with initial perturbation in the interface, and the wave length of the perturbation is larger than a certain threshold value [41], i.e., $L > 4\pi^2\sigma/(\rho_A - \rho_B)|g|$. Here σ is the surface tension coefficient and g is the gravitational acceleration. In the computational domain of $[0,L]\times[-2L,2L]$, the initial interface is located at $y_0 = 2L + \delta\cos(2\pi x/L)$, where $\delta = 0.1L$ is the amplitude of the perturbation. In this problem, the Atwood number is introduced, which is defined as $At = (\rho_A - \rho_B)/(\rho_A + \rho_B)$, and cases of $At = 0.5$ and $At = 0.98$ will be presented. The Reynolds

number is defined as $\mathrm{Re} = \rho_A L\sqrt{|gL|}/\mu$, where μ is the dynamic viscosity, and the Péclet number is defined as $Pe = L\sqrt{|gL|}/M_\phi$. We set the reference length equal to $L = 256\ lu$, and the reference time $T = \sqrt{L/|gAt|} = 16{,}000\ ts$. In addition, the surface tension coefficient is $\sigma = 5\times10^{-5}\ mu/ts^2$ and the interface width is $W = 5\ lu$.

FIG. 11 depicts five stages of the instability at $At = 0.5$, $\mathrm{Re} = 3{,}000$, and $Pe = 1{,}000$, and the same flow regime can also be found in the work of Ding *et al.* [37], Li *et al.* [31] and Zu *et al.* [23]. In this case, vortices and breakups near the rolling-up tails of the interface can be observed directly. Dimensionless positions of the spike of the falling heavy fluid (phase A) and the bubble of the rising light phase (phase B) are recorded till $t = 3.25T$ and shown in FIG. 12. It is clear that present results are in good agreement with the results of Ding *et al.* [37] and Li *et al.* [31], but show a slight deviation from the results of Zu *et al.* [23]. The interfacial patterns shown in FIG. 11 also agree well with those in [31].

During the simulation, the variations of relative maximum and minimum values of the order parameter are shown in FIG. 13, revealing low numerical dispersion even at the last stage when the value of the maximum order parameter increases rapidly.

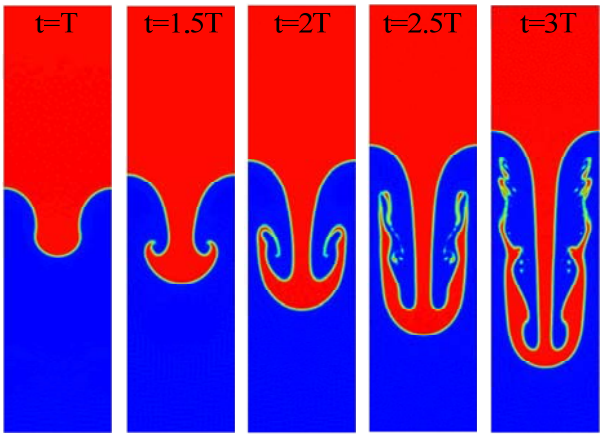

FIG. 11. Snapshots of simulation of Rayleigh-Taylor instability at $At = 0.5$, $\mathrm{Re} = 3{,}000$, and $Pe = 1{,}000$. The time is normalized by $T = \sqrt{L/|gAt|}$.

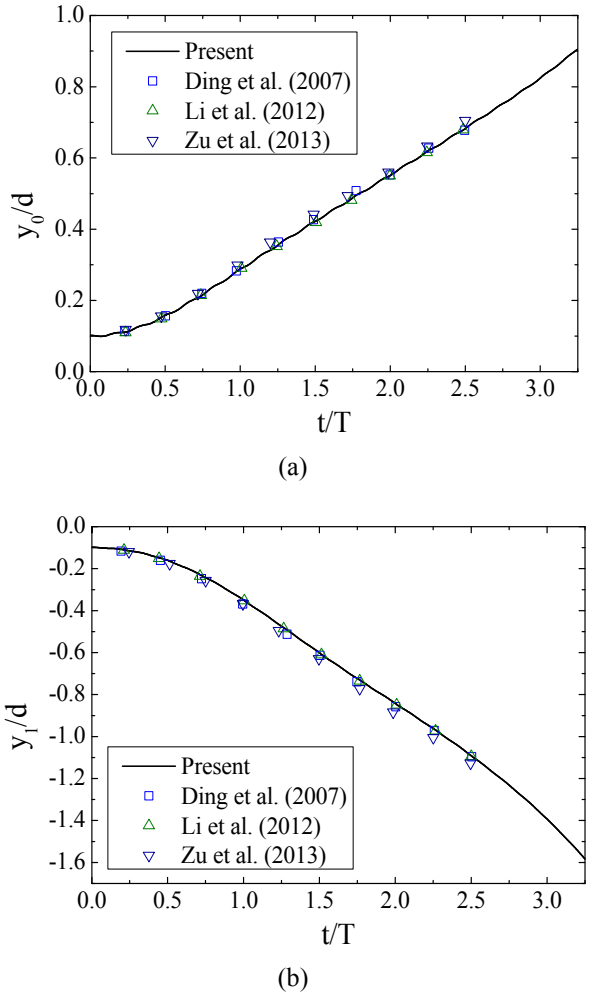

FIG. 12. Time evolution of the positions of (a) the bubble front and (b) the spike tip, and comparisons with numerical results of Ding *et al.* [37], Li *et al.* [31], and Zu *et al.*. [23].

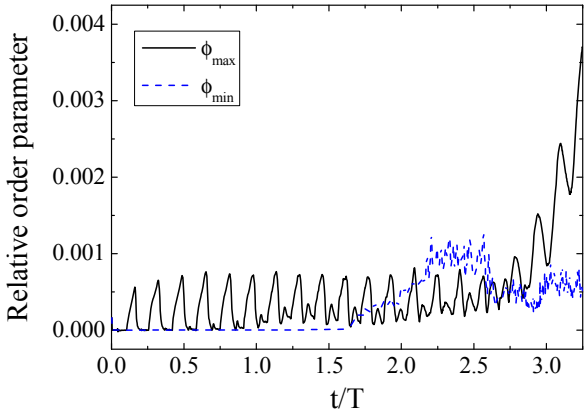

FIG. 13. Time evolution of relative maximum and minimum of the order parameter

In general, numerical instability occurs easily in cases where high density ratio is applied. Previous researchers have shown that cases with both high density ratio and high Reynolds number

can hardly be achieved at the same time [23,24,43,44]. However, the reasons have not been drawn clearly yet.

In practice, we believe that one key point is to eliminate excessive dispersion in the phase-tracking procedure. We have shown in Sec. III that the values of order parameter during simulations could be much larger than ϕ_A or smaller than ϕ_B, and this problem become worse in situations where a complex velocity field is given or large values of the Péclet number are specified. In addition, since the density is calculated linearly through the order parameter, coupling effects would also be transferred to the hydrodynamic equation.

To eliminate the numerical dispersion, one method is to apply more discretization lattice vectors, e.g., the D2Q17 model [45], and adopt higher-order discretization schemes to calculate the normal vector [20,25], which causes low computational efficiency. The other method is to suppress the range by applying a cut-off technique to the calculation of order parameter, i.e.,

$$\phi(\mathbf{x}) = \begin{cases} \phi_A & \text{, if } \phi > \phi_A \\ \phi_B & \text{, if } \phi < \phi_B \end{cases}. \tag{39}$$

While applying the cut-off technique, mass conservation in the whole system cannot be ensured. In the work of Chiu *et al.* [13], a mass compensating method is introduced to solve this problem, in which density is redistributed during every time step. However, in different situations, the rate of mass loss or mass rise might be quite variable, and we choose to track it explicitly. Herein we directly apply the cut-off technique in Rayleigh-Taylor instability at $At = 0.98$, and hence $\rho_A/\rho_B = 99$.

Interface structures are shown in FIG. 14 for two cases of different values of Reynolds number, i.e., $\mathrm{Re} = 3{,}000$ and $\mathrm{Re} = 600$. It is shown that the roll-up, induced by the secondary Kelvin-Helmholtz instability [19], does not appear at large Atwood number. During the simulations, the total mass change is recorded, as shown in FIG. 15. It is clear that in these two cases, although mass loss occurs, the relative rate is below 0.2% in the whole process.

Currently very few studies of the Rayleigh-Taylor instability of immiscible fluids with high density ratio have been conducted, and similar situation at $At = 0.999$ and $\mathrm{Re} = 200$ was investigated by Shao et al. [35], where higher-order FDM was adopted for the phase-field equation. The current model fails in this situation, however, through the results illustrated in FIG. 14 and FIG. 15, the current model reveals satisfying numerical stability when dealing with high density ratio problems, and achieves much larger values of the Reynolds number. In addition, the current model fails to simulate some important situations, such as the water-air system, where the density ratio is around 800, and the dynamic viscosity ratio is around 58. Further work is still needed to solve problems concurrently involving high density ratio, high viscosity ratio, and high-Re conditions.

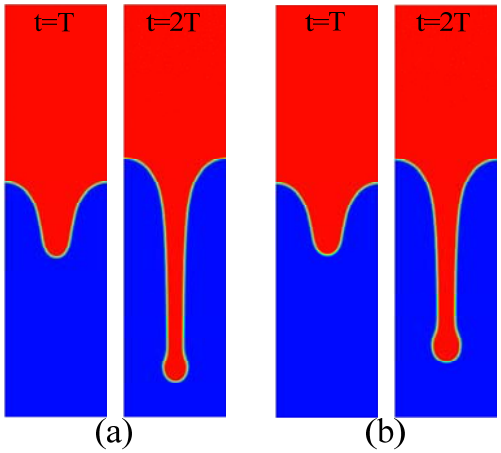

FIG. 14. Snapshots of simulation of Rayleigh-Taylor instability at: (a) $At = 0.98$, $\mathrm{Re} = 3,000$, and $Pe = 600$; (b) $At = 0.98$, $\mathrm{Re} = 600$, and $Pe = 600$.

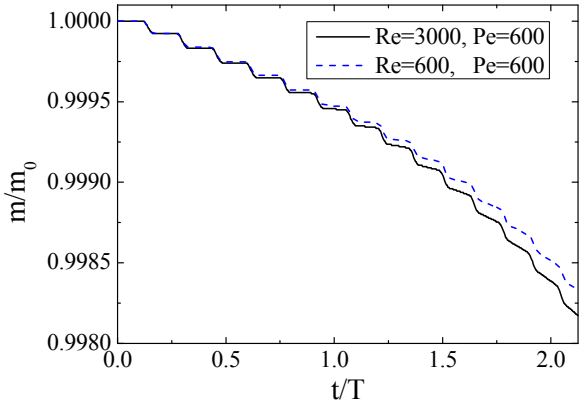

FIG. 15. Time evolution of total mass when applying the cut-off technique to the order parameter at $At = 0.98$.

V. SUMMARY

In this article, we propose a phase-field-based Lattice Boltzmann model to track the interfaces of binary flow systems. Through the Chapman-Enskog analysis, the correct form of the conservative ACE is recovered. Since the conservative ACE involves a lower-order diffusion term compared with the CHE, better accuracy and lower numerical dispersion are expected.

In the interface-tracking tests, our improved model shows satisfying performance when considering the effect of the CFL number and the Péclet number, the convergence rate, and numerical dispersion. In the binary flow tests, our model is coupled with the hydrodynamic equation developed by Liang *et al.* [24]. In the cases of layered Poiseuille flow, the numerical results of the velocity profiles agree well with analytical results for high viscosity ratio situations. And in the Rayleigh-Taylor instability simulations, both high density ratio and high Reynolds number are successfully simulated to illustrate the model's capacity in dealing with complicated situations.

To conclude, this article provides a simple and reliable solution for the phase-field modeling of binary flows. Moreover, extensions to other lattice models, e.g., the D2Q5 and D3Q7 models, are

straightforward.

ACKNOWLEDGEMENTS

This article is supported by the Young Scientists Fund of the National Science Foundation of China (Grant No. 11502210), and the Innovation Foundation for Doctor Dissertation of Northwestern Polytechnical University (Grant No. CX201501). The first author also receives financial funding from China Scholarship Council. This material is based upon work supported by the National Science Foundation (Grant No. EAR-1204762). The authors acknowledge the Instructional & Research Computing Center at Florida International University for providing the High Performance Computing (HPC) resource, and we are grateful for assistance from Dr. Mengxing Cheng, the HPC administrator.

APPENDIX A: Chapman-Enskog analysis

In Eq. 18, the equilibrium function and source terms in moment space are listed as

$$\mathbf{m}_{eq}^{h}=\mathbf{M}\mathbf{h}^{eq}=\left[\phi,2\phi,-2\phi,\phi u_x,-\phi u_x,\phi u_y,-\phi u_y,0,0\right]^T, \tag{A1}$$

$$\mathbf{m}_{S}^{h}=\mathbf{M}\mathbf{S}^{h}=\left[0,0,0,\theta c_s^2 n_x,-\theta c_s^2 n_x,\theta c_s^2 n_y,-\theta c_s^2 n_y,0,0\right]^T, \text{ and} \tag{A2}$$

$$\mathbf{m}_{R}^{h}=\mathbf{M}\mathbf{R}=\left[0,0,0,\partial_t\phi u_x,-\partial_t\phi u_x,\partial_t\phi u_y,-\partial_t\phi u_y,0,0\right]^T. \tag{A3}$$

Here the matrix $\mathbf{M}$ can be found in Ref. [17,24,35,43,44]. By multiplying Eq. 18 by matrix $\mathbf{M}$, we have

$$\mathbf{m}^{h}\left(\mathbf{x}+\mathbf{e}_i\delta t,t+\delta t\right)-\mathbf{m}^{h}\left(\mathbf{x},t\right)=-\boldsymbol{\Lambda}^{h}\left[\mathbf{m}^{h}\left(\mathbf{x},t\right)-\mathbf{m}_{eq}^{h}\right]+\left(\mathbf{I}-\boldsymbol{\Lambda}^{h}/2\right)\left(\mathbf{m}_{S}^{h}+\mathbf{m}_{R}^{h}\right)\delta t. \tag{A4}$$

Applying the Taylor expansion to Eq. (A4) and using the Chapman-Enskog expansion $\partial_t=\varepsilon\partial_{t1}+\varepsilon^2\partial_{t2}$, $\nabla=\varepsilon\nabla_1$, and $\mathbf{m}=\mathbf{m}^{(0)}+\varepsilon\mathbf{m}^{(1)}+\varepsilon^2\mathbf{m}^{(2)}$, where $\varepsilon=\delta t$, we have

$$\hat{\mathbf{D}}\mathbf{m}^{h}+\frac{\delta t}{2}\hat{\mathbf{D}}^2\mathbf{m}^{h}=-\frac{\boldsymbol{\Lambda}^{h}}{\delta t}\left[\mathbf{m}^{h}\left(\mathbf{x},t\right)-\mathbf{m}_{eq}^{h}\right]+\left(\mathbf{I}-\frac{\boldsymbol{\Lambda}^{h}}{2}\right)\left(\mathbf{m}_{S}^{h}+\mathbf{m}_{R}^{h}\right), \tag{A5}$$

where $\hat{\mathbf{D}}=\mathbf{I}\partial_t+\mathbf{E}\cdot\nabla$, and $\mathbf{E}=\mathbf{M}\cdot diag\left(\mathbf{e}_0,\mathbf{e}_1,\cdots,\mathbf{e}_8\right)\cdot\mathbf{M}^{-1}$.

Retaining terms to scale $O\left(\varepsilon^2\right)$ in scales $O\left(\varepsilon^0\right)$, $O\left(\varepsilon^1\right)$, and $O\left(\varepsilon^2\right)$, Eq. (A5) yields

$$O\left(\varepsilon^0\right):\mathbf{m}^{h(0)}=\mathbf{m}_{eq}^{h}, \tag{A6a}$$

$$O\left(\varepsilon^1\right):\hat{\mathbf{D}}_1\mathbf{m}^{h(0)}=-\frac{\boldsymbol{\Lambda}^{h}}{\delta t}\mathbf{m}^{h(1)}+\left(\mathbf{I}-\frac{\boldsymbol{\Lambda}^{h}}{2}\right)\left(\mathbf{m}_{S}^{h}+\mathbf{m}_{R}^{h(1)}\right), \tag{A6b}$$

$$O\left(\varepsilon^2\right):\partial_{t2}\mathbf{m}^{h(0)}+\hat{\mathbf{D}}_1\left(\mathbf{I}-\frac{\mathbf{\Lambda}^h}{2}\right)\left[\mathbf{m}^{h(1)}+\frac{\delta t}{2}\left(\mathbf{m}_S^h+\mathbf{m}_R^{h(1)}\right)\right]=-\frac{\mathbf{\Lambda}^h}{\delta t}\mathbf{m}^{h(2)}+\left(\mathbf{I}-\frac{\mathbf{\Lambda}^h}{2}\right)\mathbf{m}_R^{h(2)}. \quad \text{(A6c)}$$

To deduce the corresponding equation, we write the separated equations for the conserved moment m_0^h in scales $O\left(\varepsilon^0\right)$, $O\left(\varepsilon^1\right)$, and $O\left(\varepsilon^2\right)$ as

$$O\left(\varepsilon^0\right):m_0^{h(0)}=\phi, \quad \text{(A7a)}$$

$$O\left(\varepsilon^1\right):\partial_{t1}\phi+\nabla_1\cdot\begin{pmatrix}\phi u_x\\ \phi u_y\end{pmatrix}=0\text{, and} \quad \text{(A7b)}$$

$$O\left(\varepsilon^2\right):\partial_{t2}\phi+\nabla_1\cdot\begin{bmatrix}\left(1-s_3^h/2\right)\cdot m_3^{h(1)}\\ \left(1-s_5^h/2\right)\cdot m_5^{h(1)}\end{bmatrix}+\frac{\delta t}{2}\nabla_1\cdot\begin{bmatrix}\left(1-s_3^h/2\right)\cdot\left(\theta c_s^2 n_x+\partial_{t1}\phi u_x\right)\\ \left(1-s_5^h/2\right)\cdot\left(\theta c_s^2 n_y+\partial_{t1}\phi u_y\right)\end{bmatrix}=0. \quad \text{(A7c)}$$

The separated equations for the conserved moments m_3^h and m_5^h from Eq. (A6b) in scale $O\left(\varepsilon^1\right)$ are written as

$$O\left(\varepsilon^1\right):\partial_{t1}\phi u_x+\partial_{x1}\phi c_s^2=-\frac{s_3^h}{\delta t}m_3^{h(1)}+\left(1-\frac{s_3^h}{2}\right)\left(\theta c_s^2 n_x+\partial_{t1}\phi u_x\right)\text{, and} \quad \text{(A8a)}$$

$$O\left(\varepsilon^1\right):\partial_{t1}\phi u_y+\partial_{y1}\phi c_s^2=-\frac{s_3^h}{\delta t}m_5^{h(1)}+\left(1-\frac{s_5^h}{2}\right)\left(\theta c_s^2 n_y+\partial_{t1}\phi u_y\right). \quad \text{(A8b)}$$

Now we substitute Eq. (A8a) and Eq. (A8b) into Eq. (A7c) and we can obtain

$$\partial_{t2}\phi+\delta t\nabla_1\cdot\begin{bmatrix}\left(1-s_3^h/2\right)\cdot\left(-\partial_{x1}\phi c_s^2+\theta c_s^2 n_x\right)\\ \left(1-s_5^h/2\right)\cdot\left(-\partial_{y1}\phi c_s^2+\theta c_s^2 n_y\right)\end{bmatrix}=0. \quad \text{(A9)}$$

For isotropic-diffusion systems, we have $s_3^h=s_5^h$. Combining Eq. (A7b) and Eq. (A9) together gives the correct form of the conservative ACE, i.e.,

$$\partial_t\phi+\nabla\cdot\left(\phi\mathbf{u}\right)=M_\phi\left[\nabla^2\phi-\nabla\cdot\left(\theta\mathbf{n}\right)\right], \quad \text{(A10)}$$

where $M_\phi=\left(1/s_3^h-0.5\right)c_s^2\delta t$ is the mobility.

APPENDIX B: D3Q15 MODEL IN MOMENT SPACE

In the D3Q15 model, the values of the weighing factors are $w_0=2/9$, $w_{1\sim6}=1/9$, and $w_{7\sim14}=1/72$, and the corresponding lattice vectors are

$$\mathbf{e} = c\begin{bmatrix} 0 & 1 & -1 & 0 & 0 & 0 & 0 & 1 & -1 & 1 & -1 & 1 & -1 & 1 & -1 \\ 0 & 0 & 0 & 1 & -1 & 0 & 0 & 1 & 1 & -1 & -1 & 1 & 1 & -1 & -1 \\ 0 & 0 & 0 & 0 & 0 & 1 & -1 & 1 & 1 & 1 & 1 & -1 & -1 & -1 & -1 \end{bmatrix}. \quad \text{(B1)}$$

Similar to the D2Q9 model, the equilibrium function and source terms in moment space for the D3Q15 model are listed as

$$\mathbf{m}_{eq}^{h} = \left[\phi, -\phi, \phi, \phi u_x, -7\phi u_x/3, \phi u_y, -7\phi u_y/3, \phi u_z, -7\phi u_z/3, 0, 0, 0, 0, 0, 0\right]^T, \quad \text{(B2)}$$

$$\mathbf{m}_{S}^{h} = \left[0, 0, 0, \phi c_s^2 n_x, -7\phi c_s^2 n_x/3, \phi c_s^2 n_y, -7\phi c_s^2 n_y/3, \phi c_s^2 n_z, -7\phi c_s^2 n_z/3, 0, 0, 0, 0, 0, 0\right]^T, \text{ and} \quad \text{(B3)}$$

$$\mathbf{m}_{R}^{h} = \left[0, 0, 0, \partial_t \phi u_x, -7\partial_t \phi u_x/3, \partial_t \phi u_y, -7\partial_t \phi u_y/3, \partial_t \phi u_z, -7\partial_t \phi u_z/3, 0, 0, 0, 0, 0, 0\right]^T. \quad \text{(B4)}$$

The transformation matrix $\mathbf{M}$ for the D3Q15 model, which is used to derive these terms, can be found in Ref. [43].

REFERENCES

[1] C. Pan, L. S. Luo, and C. T. Miller, Comput. Fluids **35**, 898 (2006).

[2] D. Bonn, J. Eggers, J. Indekeu, and J. Meunier, Rev. Mod. Phys. **81**, 739 (2009).

[3] Y. Sui, H. Ding, and P. D. M. Spelt, Annu. Rev. Fluid Mech. **46**, 97 (2014).

[4] A. L. Yarin, Annu. Rev. Fluid Mech. **38**, 159 (2006).

[5] R. Scardovelli and S. Zaleski, Annu. Rev. Fluid Mech. **31**, 567 (1999).

[6] C. W. Hirt and B. D. Nichols, J. Comput. Phys. **39**, 201 (1981).

[7] D. Adalsteinsson and J. A. Sethian, J. Comput. Phys. **118**, 269 (1995).

[8] S. O. Unverdi and Grétar Tryggvason, J. Comput. Phys. **100**, 25 (1992).

[9] G. Caginalp, Arch. Ration. Mech. Anal. **92**, 205 (1986).

[10] J. Kim, Commun. Comput. Phys. **12**, 613 (2012).

[11] F. Xiao and T. Yabe, J. Comput. Phys. **170**, 498 (2001).

[12] J. W. Cahn, C. M. Elliott, and A. Novick-Cohen, Eur. J. Appl. Math. **7**, 287 (1996).

[13] P.-H. Chiu and Y.-T. Lin, J. Comput. Phys. **230**, 185 (2011).

[14] Y. Sun and C. Beckermann, J. Comput. Phys. **220**, 626 (2007).

[15] C. Mattiussi, J. Comput. Phys. **133**, 289 (1997).

[16] S. Chen and G. D. Doolen, Annu. Rev. Fluid Mech. **30**, 329 (1998).

[17] H. Haibo, M. C. Sukop, and X.-Y. Lu, Multiphase Lattice Boltzmann Methods (Wiley, 2015).

[18] M. C. Sukop and D. T. Thorne, Lattice Boltzmann Modeling: An Introduction for Geoscientists and Engineers (Springer Berlin Heidelberg, Verlag Berlin Heidelberg, 2006).

[19] X. He, S. Chen, and R. Zhang, J. Comput. Phys. **152**, 642 (1999).

[20] T. Lee and C. L. Lin, J. Comput. Phys. **206**, 16 (2005).

[21] H. W. Zheng, C. Shu, and Y. T. Chew, J. Comput. Phys. **218**, 353 (2006).

[22] H. W. Zheng, C. Shu, Y. T. Chew, and J. H. Sun, Int. J. Numer. Methods Fluids **56**, 1653 (2008).

[23] Y. Q. Zu and S. He, Phys. Rev. E **87**, 043301 (2013).

[24] H. Liang, B. C. Shi, Z. L. Guo, and Z. H. Chai, Phys. Rev. E **89**, 055320 (2014).

[25] H. Liang, Z. H. Chai, B. C. Shi, Z. L. Guo, and T. Zhang, Phys. Rev. E **90**, 063311 (2014).

[26] H. Liang, B. C. Shi, and Z. H. Chai, Phys. Rev. E **93**, 013308 (2016).
[27] M. Geier, A. Fakhari, and T. Lee, Phys. Rev. E **91**, 063309 (2015).
[28] A. Fakhari, M. Geier, and T. Lee, J. Comput. Phys. **315**, 434 (2016).
[29] Z. Guo, B. Shi, and N. Wang, J. Comput. Phys. **165**, 288 (2000).
[30] S. Osher and R. Fedkiw, Lvel Set Methods and Dynamic Implicit Surfaces (Springer, 2002).
[31] Q. Li, K. H. Luo, Y. J. Gao, and Y. L. He, Phys. Rev. E **85**, 026704 (2012).
[32] J. Kim, J. Comput. Phys. **204**, 784 (2005).
[33] J. Chao, R. Mei, R. Singh, and W. Shyy, Int. J. Numer. Methods Fluids **66**, 622 (2011).
[34] C. Shu and S. Osher, J. Comput. Phys. **77**, 439 (1988).
[35] J. Y. Shao and C. Shu, Int. J. Numer. Methods Fluids **77**, 526 (2015).
[36] S. Gottlieb and C. Shu, Math Comp **67**, 73 (1998).
[37] H. Ding, P. D. M. Spelt, and C. Shu, J. Comput. Phys. **226**, 2078 (2007).
[38] Q. Kang, D. Zhang, and S. Chen, Adv. Water Resour. **27**, 13 (2004).
[39] I. Ginzburg, J. Stat. Phys. **126**, 157 (2007).
[40] M. L. Porter, E. T. Coon, Q. Kang, J. D. Moulton, and J. W. Carey, Phys. Rev. E **86**, 036701 (2012).
[41] F. Charru, Hydrodynamic Instabilities (Cambridge Press, 2011).
[42] H. Liang, Q. X. Li, B. C. Shi, and Z. H. Chai, Phys. Rev. E **93**, 033113 (2016).
[43] K. N. Premnath and J. Abraham, J. Comput. Phys. **224**, 539 (2007).
[44] A. Fakhari and T. Lee, Phys. Rev. E **87**, 023304 (2013).
[45] L. Zheng, B. Shi, and Z. Guo, Phys. Rev. E **78**, 026705 (2008).